

Tailoring the weight of surface and intralayer edge states to control LUMO energies

Sarah Jasmin Finkelmeyer^{1,2}, Erik J. Askins^{3,4}, Jonas Eichhorn⁵, Soumik Ghosh^{1,2,6}, Carmen Siegmund⁷, Eric Täuscher⁷, Andrea Dellith¹, Maximilian L. Hupfer¹, Jan Dellith¹, Uwe Ritter⁷, Joseph Strzalka⁸, Ksenija Glusac^{3,4}, Felix H. Schacher^{5,9,10}, Martin Presselt^{1,6,10,*}

¹ Leibniz Institute of Photonic Technology (IPHT), Albert-Einstein-Str. 9, 07745 Jena, Germany

² Institute of Physical Chemistry, Friedrich Schiller University Jena, Helmholtzweg 4, 07743 Jena, Germany.

³ Department of Chemistry, University of Illinois Chicago, 845 West Taylor Street, Chicago, Illinois 60607, United States.

⁴ Chemical Sciences and Engineering Division, Argonne National Laboratory, 9700 S. Cass Avenue, Lemont, Illinois 60439, United States.

⁵ Institute of Organic Chemistry and Macromolecular Chemistry (IOMC), Friedrich-Schiller-University Jena, Humboldtstraße 10, Jena, 07743, Germany.

⁶ sciclus GmbH & Co. KG, Moritz-von-Rohr-Str. 1a, 07745 Jena, Germany.

⁷ Institute for Chemistry and Biotechnology, Ilmenau University of Technology, 98684 Ilmenau, Germany.

⁸ X-Ray Science Division, Argonne National Laboratory, 9700 S. Cass Avenue, Lemont, IL 60439, United States.

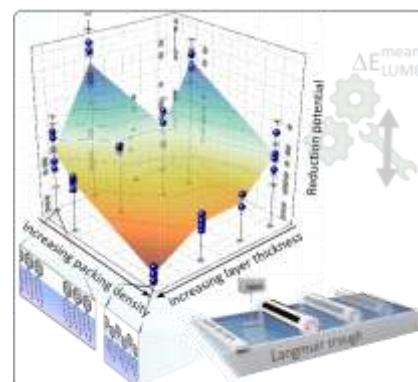
⁹ Jena Center for Soft Matter (JCSM), Friedrich-Schiller-University Jena, Philosophenweg 7, 07743 Jena, Germany.

¹⁰ Center for Energy and Environmental Chemistry Jena (CEEC Jena), Friedrich Schiller University Jena, Philosophenweg 7a, 07743 Jena, Germany.

*Corresponding author: martin.presselt@leibniz-ipht.de

ABSTRACT

The energies of the frontier molecular orbitals determine the electronic and optical properties in organic films, which is crucial for their application as organic semiconductor materials, e.g., in organic solar cells, and strongly depend on the morphology and supramolecular structure. The impact of the latter two properties on the electronic energy levels relies primarily on nearest neighbor interactions, which are difficult to study in thin films due to their nanoscale nature and heterogeneity. Here we present an automated method for fabricating layered thin films with a tailored ratio of surface to bulk sites and a controlled extent of domain edges within the layers, both of which we use to control nearest neighbor interactions. This method uses a Langmuir-Schaefer-type rolling transfer of Langmuir layers (rtLL) to minimize flow during deposition of rigid Langmuir layers composed of π -conjugated molecules. Using UV-vis absorption spectroscopy, atomic force and transmission electron microscopy we show that the rtLL method significantly advanced the deposition of multi-Langmuir layers and enables the production of films with highly



This article has been accepted for publication and undergone full peer review but has not been through the copyediting, typesetting, pagination and proofreading process, which may lead to differences between this version and the [Version of Record](#). Please cite this article as [doi: 10.1002/adma.202305006](https://doi.org/10.1002/adma.202305006).

This article is protected by copyright. All rights reserved.

defined morphology. The variation in nearest neighbor interactions thus achieved and the resulting systematically tuned lowest unoccupied molecular orbital (LUMO) energies (determined via square wave voltammetry) enabled us to establish a handy model that functionally relates the LUMO energies to a morphological descriptor, allowing for prediction of the range of experimentally accessible LUMO energies.

1. Introduction

As the understanding of the role of morphologies^[1] and energy levels^[2] of organic solar cells has been successively improved, their power conversion efficiencies and longevity have also been steadily enhanced.^[3] In the course of this progress, various approaches have been taken to control the morphology and supramolecular structures, such as improving material design to tailor supramolecular assemblies for ideal charge separation^[4] and charge transport properties^[5], but also special deposition techniques for tailoring morphologies have been developed, such as meniscus-guided deposition techniques and others.^[6] The resulting morphologies and supramolecular structures crucially determine optical and electronic material properties^[7], that can be qualitatively understood by considering nearest neighbor interactions involving mutual orientations^[8], intermolecular distances and number of nearest neighbors.^[8b, 9]

Fernandez-Torrente et al.^[9b] and Das et al.^[8b] attempted to gain a deeper understanding of morphology-property relations by investigating the influence of nearest neighbor interactions on frontier energy levels and open circuit voltages. Das et al.^[8b] varied the nearest-neighbor interactions by using multiple film morphologies prepared by different techniques and observed impressive variation of the lowest unoccupied molecular orbital (LUMO) energies by approximately 120 meV, i.e., supramolecular variation led to a three-times larger LUMO energy difference compared to C₆₀ and C₇₀^[8b] (30-40 meV^[10]). To functionally link and enable prediction of average LUMO energies (E_{LUMO}^{mean}) in thin films with a morphological descriptor, the authors^[8b] derived a simple model (Eq. 1) that describes E_{LUMO}^{mean} as a function of the morphology descriptor, defined as the ratio between the number of molecules in surface (N^{surf}) and bulk sites (N^{bulk}).

$$E_{LUMO}^{mean} = E_{LUMO}^{bulk} + \frac{\Delta N_{nn} \Delta E_{LUMO}}{1 + \frac{N^{bulk}}{N^{surf}}} \quad (\text{Eq. 1})$$

where ΔN_{nn} is the difference between numbers of nearest neighbors (N_{nn}) for the surface and bulk sites, and ΔE_{LUMO} is the LUMO energy stabilization imposed through each nearest neighbor interaction.

Assuming that any stable morphology is dominated by a distinct supramolecular structure, $\Delta N_{nn} \Delta E_{LUMO}$ may be considered approximately constant throughout the thin film. Then, the average LUMO energy can be described depending on the ratio $\frac{N^{bulk}}{N^{surf}}$, which accounts for the different morphologies, and the parameters $\Delta N_{nn} \Delta E_{LUMO}$ and E_{LUMO}^{bulk} , where the latter refers to a minimum LUMO energy in a dense bulk.^[8b] Based on this model, knowledge of surface topography and molecular packing density would suffice to predict how frontier molecular energy levels combine to generate frontier electronic energy levels in a thin film, which is of utmost importance for molecular thin film engineering.

However, in the work of Das et al. the obtained data could not be uniformly modelled with a common parameter set for the $\frac{N^{bulk}}{N^{surf}}$ term appear in Eq. 1. Instead, distinct and extreme parameters had to be used.^[8b] The issue may have originated from the highly heterogeneous morphologies produced through different techniques. This variety of techniques, from classical lab-scale spin casting to interfacial assembly, appears ideally suited to investigate how far electronic properties can be controlled supramolecularly or morphologically but complicates modeling and is also not suitable for large-scale processes, where ideally the supramolecular structure should be tuned in respect to thermodynamic stability, charge carrier mobility, and energy level alignment in the same, scalable process.

It remains an open question exactly what the relationship between morphology and a film's electronic energy levels is. Undoubtedly, improving the description of the variable morphologies and films such that a uniform parameter set, i.e., $\frac{N^{bulk}}{N^{surf}}$, may be used for modeling will yield answers. Likewise, expanding the model to functionally relate morphologies, supramolecular structures and electronic properties is another promising avenue to study.

Among the techniques developed to control thin film morphologies and supramolecular structures, the Langmuir film deposition techniques stand out^[11], for their ability to selectively tune packing densities^[12] and surface-to-volume ratios and are in principle scalable.^[13] Consequently, for reappraising Eq. 1 we will first investigate whether Langmuir-type deposition alone enables fabrication of fullerene thin films that differ similarly substantially in LUMO energies as those presented by Das et al.^[8b] and whether the Langmuir technique yields film morphologies that can be uniformly analyzed. If the latter criterion can be fulfilled, the Langmuir technique, with the related layer-by-layer deposition, shall enable the variation of packing densities at constant surface-to-volume ratios and vice versa, which should allow evaluation and refinement of the above-mentioned model. Beyond these anticipated fundamental insights into the role of nearest neighbor, i.e., intermolecular interactions, for the position of frontier energy levels, this work will quantify to what extent supramolecular structures, morphologies, and electronic properties of practically applicable thin films can be varied using the Langmuir, and related techniques, alone. Because scalability and automation are key for industrial production and robust data acquisition, respectively, an automated rolling transfer Langmuir layer (rtLL) deposition for efficient multilayer deposition is introduced in this work. The resulting layer stacks with varied morphologies and supramolecular structures will be optically, electronically, and morphologically characterized using UV-vis transmission spectroscopy, squarewave voltammetry, transmission electron and atomic force microscopy, and grazing incidence wide angle x-ray scattering.

2. Results and discussion

2.1. Assembly to monolayers

To investigate whether supramolecular structures and morphologies can be systematically tuned using the Langmuir technique we employ the amphiphilic fullerene derivative MPEGC₆₀ (bis-polyethylene glycol malonate C₆₀) introduced above (see

Figure 1).^[8b, 14] The Langmuir isotherm (

Figure 1b) shows how surface pressure (Π), measured using a Wilhelmy balance, rises with decreasing mean molecular areas (mma). A decreasing mma corresponds to an increasing surface concentration of the water-insoluble amphiphiles (here MPEGC₆₀), thus providing control over lateral molecular intra-layer structures. The Π (mma) isotherm (

Figure 1b) rises from about mma=140 Å² towards lower mma. Between 80 Å² and 60 Å² the compression modulus^[15] (C_s^{-1}) of MPEGC₆₀ reaches its maximum ($C_s^{-1} \geq 80$ mN/m,

Figure 1a), thus indicating rigid buckyball monolayers (cf. the liquid-to-solid phase transition of stearic acid (SA) monolayers^[15-16] at approx. 25 Å² and 80 mN/m in the gray curve in

Figure 1a). The highest rigidity of the MPEGC₆₀ Langmuir layer at $mma_c(C_s^{-1, \max}) = 68$ Å² corresponds to the inflection point in the Π (mma) isotherm being referred to as the collapse point of the monolayer.^[17] Consequently, the Langmuir technique provides a tool to systematically tune the mma from loose to dense and rigid packings at the collapse point of the monolayer.

If we consider close-packing of equal spheres within a quasi-two-dimensional monolayer (

Figure 1c2) the theoretically smallest mma for each fullerene (diameter $d = 7$ Å, intermolecular distance $d_{\text{inter}} = 3$ Å)^[9a, 14] amounts to

$$mma_{C,2D\text{-theo}} = ((7+3) \text{ \AA} \pm 0.5 \text{ \AA})^2 \cdot \sin(60^\circ) = (87 \pm 9) \text{ \AA}^2 \text{ (Eq. 2).}$$

The error in the fullerene unit cell lengths of 0.5 Å accounts for variations in intermolecular distances possible at room temperature according to the theoretical work of Das et al.^[8b] Consequently, rigid monolayers that are compressed to the collapse point ($mma_c < mma_{C,2D\text{-theo}}$) below the theoretical minimum in-plane mma must feature supramolecular structures that are more densely packed than the perfect 2D-monolayers shown in

Figure 1c2, e.g., layers where fullerenes are alternately squeezed out of plane (

Figure 1c1). A similar supramolecular structure of alternately offset fullerenes has been proposed by Wang et al.^[18] for crown-ether-functionalized derivatives. Layers at larger m_{mas} , i.e., $m_{ma} > m_{ma_{C_{60}D_{2D-theo}}$, are either less densely packed or are composed of densely packed domains, as illustrated in

Figure 1c3-4. Consequently, targeting m_{mas} between 120 \AA^2 and 75 \AA^2 , or the corresponding surface pressures, respectively, provides a systematic means of varying supramolecular structures or morphologies via the Langmuir technique.

2.2. Deposition of Langmuir layers

Langmuir and Blodgett developed the eponymous Langmuir-Blodgett (LB) deposition technique as a way to systematically vary film thicknesses while maintaining uniformity throughout each independent layer for a given supramolecular structure.^[11, 19] In the LB method, a floating Langmuir layer is compressed to a constant surface pressure ($\Pi_{dep} = \text{const.}$) by constraining the interfacial area available to the layer which is then deposited onto a substrate by vertical up- or downstrokes, thereby maintaining the surface pressure constant through feed-back-controlled feed of the Langmuir layer.^[11b] However, the monolayer is often only partially transferred to the immersed substrate, whose width is usually smaller than the widths of the assembled monolayer, thus causing shear in the Langmuir layer floating at the air-water interface which is critical for maintaining constant surface pressure and film uniformity during deposition.^[17c, 20]

As an alternative technique, Langmuir and Schaefer (LS)^[21] developed the horizontal lift-off method. Here, the lipophilic surface of the Langmuir layer must adhere to the substrate for deposition. Although a single LS deposition does not require feed or flow of the Langmuir layer (LL) during deposition, transfer of multiple layers with the classical LS technique at the same local area at the air-water interface requires flowing of the LL into the nascent vacancy generated in the LL after its partial deposition on the small substrates. For the MPEG_{C₆₀} fullerenes studied in this work, the described obstacles result in inhomogeneous morphologies of LB and LS films (Figure SI 2 a-c), LB transfer ratios that are strongly scattering with successive deposition from the same spot (Figure SI 2 d,e), and decreasing UV-vis absorption per layer (Figure SI 2 f-i).

To circumvent the need for notable LL flow at deposition and to automate LS-type multilayer deposition at systematically varied sections of the LL at constant surface pressure, we developed a rolling transfer Langmuir layer (rtLL) deposition technique, which is illustrated in Figure 2 (cf. other LB-related techniques that involve rolls.^[13a-c, 13e, 13f, 22]).

Using this rtLL technique, multiple layers of specific supramolecular structures with highly homogeneous morphologies could be efficiently produced (Figs SI 5 - 6), which is crucial to systematically research and understand the influence of nearest neighbor interactions on the electronic properties of the resulting films. Particularly, the new automated rtLL deposition method

provides reproducibly fabricated and tailored films for detailed investigation of the dependence of LUMO energies on the ratio between MPEGC₆₀ molecules in bulk and surface sites and on the deposition pressure.

2.3. Range of reduction potential and LUMO energy variation

To investigate whether Langmuir-type fullerene assembly by rtLL deposition yields supramolecular structures and film morphologies that give rise to similarly large LUMO energy variations as reported in literature^[8b], where different film production techniques were employed, MPEGC₆₀ Langmuir layers are deposited at systematically varied packing densities, i.e., deposition surface pressures, and varied layer numbers. The reduction potentials determined via square wave voltammetry (Figure 3) show a strong dependence on the number of stacked rtLLs and the deposition pressure Π_{rtLL} . The most negative reduction potential vs. vacuum energy (referred as E_{LUMO}^{mean} ^[23] in the following) is obtained for the highest packing density ($\Pi_{rtLL}=15$ mN/m, #rtLL=36: $E_{LUMO,min}^{mean}=-4.12$ eV), i.e., the largest deposition pressure, and the largest number of rtLLs. The least negative reduction potentials are measured for the fewest number of layers and a medium packing density (#rtLL=4, $\Pi_{rtLL}=5$ mN/m: $E_{LUMO,max}^{mean}=-4.04$ eV) and for the loosest packing (#rtLL=24, $\Pi_{rtLL}=1.2$ mN/m: $E_{LUMO}^{mean}=-4.05$ eV), thus resulting in a LUMO energy variation of 0.08 eV (80 meV) achieved with the Langmuir technique alone.

Compared to the LUMO energy variation of 120 meV reached through employing various film production methods,^[8b] the variation in film morphologies and supramolecular structures via the rtLL method is more systematic and shall facilitate developing models that connect morphological and supramolecular descriptors with electrochemical properties. Importantly, the rtLL deposition technique facilitates sample fabrication as it enables automatized coating of several substrates (according to the number of substrates mounted to the roll), thus allowing parallel production of multiple samples at identical Π_{rtLL} and, if desired, varied #rtLL-values. The sample series that was produced using the rtLL technique contained duplicates to yield robust electrochemical and morphological data sets. The blue spheres shown in Figure 3 represent individual samples and the black error bars show the standard deviation of the peak-fits used to determine the reduction peak maxima of each rtLL film. Individual squarewave voltammograms (Figure SI 18 to Figure SI 27) reveal that reduction peaks become narrower, better resolved, and shift to more negative potentials as discussed above, i.e., to lower E_{LUMO}^{mean} , with increasing #rtLL and Π_{rtLL} .

In the model introduced in Eq. 1, E_{LUMO}^{mean} is described to be dependent on the number of molecules in surface (N^{surf}) and bulk sites (N^{bulk}), as well as $\Delta N_{nn} \Delta E_{LUMO}$ and E_{LUMO}^{bulk} . Although the numbers of surface and bulk sites might be taken directly from the rtLL parameters in Figure 3, the morphologies and supramolecular structures of the films are investigated experimentally in detail using samples with mean molecular area $A = 117, 96, \text{ and } 78 \text{ \AA}^2$, thus revealing the structural details discussed above on the basis of the $\Pi(\text{mma})$ isotherm, see

Figure 1.

2.4. Morphological and supramolecular structure variation in rtLL films

Transmission electron microscopy (TEM) images of deposited MPEGC₆₀ monolayers (Figure SI 16) confirm the formation of islands of similar packing densities at low deposition surface pressures ($\Pi_{rtLL}=1.2$ mN/m), discussed above for interpretation of the isotherms ($mma > 90 \text{ \AA}^2$, $\Pi < 10$ mN/m,

Figure 1). At larger surface pressures ($\Pi_{rtLL}=15$ mN/m) the LS layers show a uniform density in areas larger than $0.01 \mu\text{m}^2$ (Figure SI 16c). Grazing incidence wide angle x-ray scattering (GIWAXS) measurements have been performed for multi-rtLL systems to probe the structural parameters of layered rtLL films (see Figure SI 17). The 2D GIWAXS diffraction pattern of the rtLL films deposited at $\Pi_{rtLL}=15$ mN/m show discrete reflections that are particularly pronounced for the film composed of 36 rtLL. These reflections are extended along the polar angle in the detector plane^[24], thus indicating textured polycrystallinity. Although the photographs of the films in Figure SI 5 show largely homogenous and flat MPEGC₆₀ rtLL films, lines parallel to the longitudinal edge of the substrates appear upon increasing Π_{rtLL} and #rtLL, which are interpreted as signatures of the GIWAXS-detected polycrystallinity. We attribute these lines to Langmuir layer distortions during deposition because a small mismatch between the distance covered by a full turn of the roll and the circumferences of the roll with the mounted planar substrates. These distortions are minimized through choosing narrow substrates to best resemble the curvature of the roll with the assembled substrates

Atomic force microscopy (AFM) topographies shown in Figure 4 were analyzed to determine surface roughness, areas, and number of surface molecules $N^{surface}$. The analysis of the AFM-determined topographical surface areas (A_{AFM}) reveals that these topographical surface areas are only little larger than the corresponding image sections areas (see Table SI 2). Consequently, the films can be considered very smooth, regardless of the small film distortions. This smoothness is an important prerequisite to determine the numbers of molecules in the individual layers of the rtLL films with uniform accuracy.

As detailed in the SI, the number of surface molecules was calculated by dividing A_{AFM} by the average area demanded by each molecule in the surface layer. The latter can be determined directly from the Langmuir isotherm at the point of deposition, mma_{rtLL} , and thus relates to the Langmuir layer floating at the air-water interface. This results in:

$$N_{\Pi}^{surface} = \frac{A_{AFM}}{mma_{\Pi}} \quad (\text{Eq. 3}).$$

To account for the deposition process, mma can be derived as the inverse surface concentration following a Lambert-Beer-type approach, as detailed in SI chapter 1.1:

$$\varepsilon(\lambda) = \frac{Abs(\lambda) \cdot N_A \cdot mma_{Abs}}{\#LL} \quad (\text{Eq. 4}).$$

Rewriting Eq. 4 yields

$$\frac{1}{mma_{Abs}} = \frac{Abs(\lambda) \cdot N_A}{\varepsilon(\lambda) \cdot \#LL} \quad (\text{Eq. 5}),$$

and employing mma_{Abs} (Eq. 5) instead of mma_{Π} in Eq. 3 we obtain

$$N_{Abs}^{surface} = \frac{A_{AFM}}{mma_{Abs}}. \quad (\text{Eq. 6}).$$

Eq. 6 allows us to calculate the number of molecules in the surface of deposited layer stacks when ϵ is chosen as a constant reference value (we will use $\epsilon_{\text{solution,max}}=(97024\pm544)$ L/(mol·cm), see Fig. SI 4 and Table SI 3) to account for possibly incomplete layer transfer from the air-water interface to the substrate, as indicated by varying absorption.

Similarly, the total number of molecules in the films can be calculated according $N_{\Pi}^{total} = \frac{A_{sec} \cdot \#LL}{mma_{\Pi}}$ and $N_{Abs}^{total} = \frac{A_{sec} \cdot \#LL}{mma_{Abs}}$, where A_{sec} -areas are the image section areas shown in Figure 4. The resulting ratios that are either based on isotherm- or UV-vis absorption spectra-derived lateral molecular concentrations and read as:

$$\frac{N_{\Pi}^{surface}}{N_{\Pi}^{total}} = \frac{A_{AFM} \pm \Delta A_{AFM}}{mma_{\Pi} \pm \Delta mma_{\Pi}} \cdot \frac{mma_{\Pi} \pm \Delta mma_{\Pi}}{A_{sec} \cdot \#LL} = \frac{A_{AFM}}{A_{sec} \cdot \#LL} \pm \Delta \frac{N_{\Pi}^{surface}}{N_{\Pi}^{total}} \quad (\text{Eq. 7}) \text{ and}$$

$$\frac{N_{Abs}^{surface}}{N_{Abs}^{total}} = \frac{A_{AFM} \pm \Delta A_{AFM}}{mma_{Abs} \pm \Delta mma_{Abs}} \cdot \frac{mma_{Abs} \pm \Delta mma_{Abs}}{A_{sec} \cdot \#LL} = \frac{A_{AFM}}{A_{sec} \cdot \#LL} \pm \Delta \frac{N_{Abs}^{surface}}{N_{Abs}^{total}} \quad (\text{Eq. 8})$$

respectively. Noting that mma_{Π} and mma_{Abs} appear in both numerator and denominator of equations 7 and 8, respectively, identical ratios are seen for both approaches, however their uncertainties differ. Δmma_{Π} values originate from averaging isotherms, Δmma_{Abs} refers to the reproducibility studies discussed in chapter 1 of the SI, and ΔA_{AFM} results from averaging forward and backward scans. The uncertainties of the number ratios are calculated through error propagation, as detailed in chapter 6 in the SI, and are larger for absorption- than for isotherm-derived values, particularly for low layer numbers $\#rLL$, as shown in Figure 4. In the following connection between the morphological descriptor $N^{surface}/N^{total}$ and LUMO energies, both types of uncertainties are employed.

2.5. Relation between morphological, supramolecular and electronic properties

The model introduced above (Eq. 1) describes LUMO energies which are dependent upon the ratio between the number of molecules at surface and bulk sites, $N^{bulk}/N^{surface}$. However, we feel that using the inverse ratio $N^{surface}/N^{total}$ (N^{total} instead of N^{bulk}), thus resulting in $N^{surface}/N^{total}$ -values ranging from 0 to 1, is a handier morphology descriptor than the previously used. Using the new descriptor, Eq. 1 becomes (SI chapter 7):

$$E_{LUMO}^{mean} = E_{LUMO}^{bulk} + \frac{N^{surface} \cdot \Delta N_{nn} \Delta E_{LUMO}}{N^{total}} \quad (\text{Eq. 9}).$$

Employing $x = \frac{N^{surface}}{N^{total}}$ yields

$$E_{LUMO}^{mean} = \Delta N_{nn} \Delta E_{LUMO} \cdot x + E_{LUMO}^{bulk} \quad (\text{Eq. 10}).$$

Eq. 10 represents a linear relation between the average LUMO energy, E_{LUMO}^{mean} , and the morphology descriptor $N^{surface}/N^{total}$, where $\Delta N_{nn} \Delta E_{LUMO}$ is a parameter that accounts for the supramolecular structure through the difference in nearest neighbor numbers between bulk and surface sites, ΔN_{nn} , and LUMO energy decrease per nearest neighbor interaction, ΔE_{LUMO} . In Figure

5a, the gray lines represent $E_{LUMO}^{mean}(x)$ graphs at a constant ΔE_{LUMO} of 65 meV and varying ΔN_{nn} , according to the experimental work of Fernandez-Torrente et al.^[9b] The blue line refers to $\Delta E_{LUMO} = 109$ meV according to the quantum chemical calculations of Das and co-workers^[8b] and a physical limit value of $\Delta N_{nn} = 11$. The lowest measured LUMO energy (highest packing density at $\Pi_{rtLL} = 15$ mN/m and largest $\#rtLL$ of 36) was used as E_{LUMO}^{bulk} (-4.124 eV) for all graphs in Figure 5a.

The data points in Figure 5a for densely packed films ($\Pi_{rtLL} = 15$ mN/m, $mma_{rtLL} = 78 \text{ \AA}^2$, purple symbols) approximately fall between the lines of $\Delta N_{nn}\Delta E_{LUMO} = 2 \cdot 65 \text{ meV}$ and $\Delta N_{nn}\Delta E_{LUMO} = 3 \cdot 65 \text{ meV}$, i.e., an effective LUMO energy difference between surface and bulk molecules of 130 meV to 195 meV. Depending on which value is considered for ΔE_{LUMO} , ΔN_{nn} varies between 2 and 3, which is physically reasonable for the case of dense packing of equal spheres where a bulk molecule is surrounded by 12 nearest neighbors while a molecule in a flat surface is lacking three of these neighbors, cf. the earlier work of Das et al.^[8b] If these data are fitted with the linear function defined in Eq. 10, the resulting slope $\Delta N_{nn}\Delta E_{LUMO}$ specifies the total effective LUMO energy variation possible for morphologies captured by the $N^{surface}/N^{total}$ descriptor ranging between 0 and 1.

For decreasing surface pressure at deposition (Π_{rtLL}), $\Delta N_{nn}\Delta E_{LUMO}$ increases (Figure 5b) from 150 meV ($\Pi_{rtLL} = 15$ mN/m) to 220 meV ($\Pi_{rtLL} = 5$ mN/m). As discussed above, the films deposited at low surface pressure can be composed of domains, thus resulting in surface states with reduced nearest neighbor interactions at domain edges. We propose that the resulting apparent increase in ΔN_{nn} and ΔE_{LUMO} with decreasing Π_{rtLL} , respectively, are the origins of the $\Delta N_{nn}\Delta E_{LUMO}$ variation. However, this variation is considered small as compared to the earlier work where different thin film production methods were employed to achieve LUMO energy tuning or when compared to the influence of the surface to bulk state number ratio $N^{surface}/N^{total}$ on the average LUMO energy.

The data for $\Pi_{rtLL} = 1.2$ mN/m might be approximated with $E_{LUMO}^{bulk} = -4.124$ eV and $\Delta N_{nn}\Delta E_{LUMO} = 11 \cdot 109 \text{ meV}$, the latter being unphysically large ($\Delta N_{nn}\Delta E_{LUMO} = 1.2 \text{ eV}$). A reduced slope would be obtained for stretched $N^{surface}/N^{total}$ values. Because of its non-molecular resolution, AFM systematically underestimates the surface area, which becomes more and more important with increasing roughness at decreasing deposition pressures. To circumvent this problem, extensive matrix embedding studies are presently under way.

For layers deposited as condensed films ($\Pi_{rtLL} = 5$ and 15 mN/m), we have shown here a systematic experimental tuning of LUMO energies of thin films by tailoring the weight of surface states (via $\#rtLL$) and intra-layer edge states (via Π_{rtLL}). In a theoretical work, Poelking and co-workers have shown that a similar variation (up to few hundred meV) can be expected for other dyes when ionization potentials, cf. HOMO energy, are determined as a function of the considered layer thickness.^[7] Our revised model allows the prediction of experimentally accessible tuning ranges of frontier energy levels using a small set of experimental data including a handy morphology descriptor, which could be valuable for the design of functional layers in (opto)electronic devices, such as solar cells. The rtLL deposition technique presented here provides a scalable and automated way to fabricate such layers with highest precision.

3. METHODS

Synthesis: MPEGC₆₀ was synthesized as described by Das et al.^[14].

$\Pi(A)$ isotherm characterization and Langmuir layer stack fabrication: For $\Pi(A)$ isotherm characterization, CHCl₃ (Carl Roth, ROTISOLV®, min. 99,8 %, UV/IR-Grade) solutions of MPEGC₆₀ (0.1 $\mu\text{mol/mL}$, 400 μL) were spread onto ultra-pure-water (0.2 $\mu\text{S/cm}$) subphase (temperature controlled at 25°C) of LB trough (KSV 5000, length = 520 mm, compression length = 475.2 mm, width = 150 mm). To allow complete evaporation of the solvent, 20 min are granted before starting barrier movement (10 mm/min, 2 mN/m/min) and $\Pi(A)$ isotherm recording. Four $\Pi(A)$ isotherm were recorded, averaged, and error bands were calculated. The compression modulus C_s^{-1} was calculated from the averaged isotherm by applying the formula $C_s^{-1} = -A \cdot \left(\frac{d\Pi}{dA}\right)$.^[15] A_0 was determined by extrapolating the steepest slope of the isotherm (in the range of C_s^{-1} max). Langmuir layer deposition (at different surface pressures Π : 0.5 to 15 mN/m) was carried out on a KSV NIMA Alternate Langmuir (L) and Langmuir-Blodgett (LB) trough). For LB deposition, the KSV NIMA Alternate L and LB trough-integrated dipping mechanism (alternate) was used to carry out upward stroke deposition (upstroke speed: 5 mm/min). For LS deposition, also the integrated dipping mechanism (dip) and a custom-made adapter allowing horizontal alignment of the substrate were used (dipping speed: 3 mm/min). A custom-made rolling transfer system was built for Langmuir layer deposition (rtLL: rolling-transferred Langmuir layer), consisting of a carriage-mounted roller on a V-slot driven by a custom-made controller consisting of an Arduino Nano and an A4988 stepper motor driver driving a NEMA-17 stepper motor. The roll ($\varnothing = 12$ mm) was 3D printed. The dimensions of the quartz glass substrates were 30 mm x 5 mm x 1 mm, glassy carbon substrates were 45 mm x 2.2 mm x 1 mm and silicon substrates were 20 mm x 2.2 mm x 1 mm. The rtLL velocity was 9 mm/min.

Spectroscopic investigation: UV-vis measurements were carried out using a CARY 5000 spectrometer from Varian in absorption mode within the wavelength range from 800 nm to 200 nm. UV-vis absorption measurements of fullerene solutions in chloroform were carried out in quartz glass cuvettes (obtained from Thorlabs) with a thickness of 2 mm (CV10Q700F), 4 mm (CV10Q1400F) and 10 mm (CV10Q3500F). UV-vis absorption measurements on thin films were carried out on fused silica (thickness 1000 ± 20 μm , double side polished, roughness average < 1 nm) from SIEGERT WAFER. Pure solvent in cuvettes or blank or stearic acid (SA) LB-coated quartz glasses in sample and reference beam path were used to record the baseline. Mathematica routines were used for offset-correction and for removing the spectral steps at 350 nm, caused by a light source change (Tungsten halogen to deuterium arc). First, the step at 350 nm was removed, then the spectra were smoothed via the moving average method and finally residual offsets were eliminated by setting the minimum between 750 and 800 nm to zero.

Supramolecular structure and morphological characterization: For transmission electron microscopy (TEM) measurements holey carbon film-coated copper TEM grids coated with a continuous 2 nm thin carbon membrane (QUANTIFOIL® R 2/1, 400 mesh) were cleaned by Argon plasma treatment for 120 s (Diener Electronics). Subsequently, a stearic acid (SA) monolayer was deposited ($\Pi_{\text{dep}} = 10$ mN/m) through LB-upstroke onto the Argon plasma hydrophilized carbon support. MPEGC₆₀ Langmuir layers were compressed until 1.2, 5 and 15 mN/m, respectively, and LS-type deposited at the corresponding target surface pressures onto the SA monolayer. TEM images

were acquired with a 200 kV FEI Tecnai G² 20 equipped with a 4k×4k Eagle HS CCD and a 1k×1k Olympus MegaView camera. Micrographs were adapted in terms of brightness and contrast using the software Gwyddion (2.51 version). The TEM micrograph shown in Figure SI 16e was base-flattened using the Gwyddion software and the color spread transformation was performed with the software GIMP (2.10.28 version) to maximize the contrast.

Grazing-incidence wide-angle X-ray scattering (GIWAXS) measurements were carried out at Argonne National Laboratory beamline 8-ID-E^[25] of the Advanced Photon Source. The instrument operates with x-ray photons at 10.91 keV with a beam of 200 μm x 10 μm. At incident angle $\alpha_i = 0.14^\circ$, the x-ray footprint is about 4 mm long, so the average sampling is over a spot of 4 mm x 0.2 mm. The exposure time is ~ 10 s. The sample is under vacuum during the measurement. Pilatus 1M detector is mounted 0.217 m distance to the sample, on an elevation stage that allows us to vary the detector height and record a second exposure. The two exposures can be combined to fill in the gaps of inactive pixels at the border between detector modules, thereby also demonstrating that the scattering from the sample remains constant, i.e., radiation damage does not occur in this exposure time. This procedure, as well as corrections for detector non-uniformity, x-ray polarization and geometrical solid-angle considerations, and subsequent data reduction was carried out using the GIXSGUI^[26] package for Matlab. The fullerene thin films were prepared on single side polished silicon substrates, immersed at least overnight in isopropanol before usage. One monolayer of stearic acid (SA) was LB-deposited at 10 mN·m⁻¹ prior to the rolling transferred Langmuir layers. The deposition parameters for rolling transfer of MPEGC₆₀ were 12 and 36 layers at approximately 15 mN·m⁻¹. The samples were stored under ambient conditions for shipping.

Atomic force microscopy AFM was performed on a Dimension Edge from Bruker. The silicon tip has a radius of approx. 10 nm and was used in tapping mode with a frequency of 0.4 Hz. Resolution was 512 pixel x 512 pixel. The post-processing of the data was performed with the Gwyddion software (2.51 version). For the topography images, the following processing steps were performed: “base flatten”, “align rows” with the selection mean of differences, “remove scars”, “polynomial background”, set minimum value as zero point (“fix zero”). The color scale was used in a fixed range. The actual area was read out via the “statistical quantities tool”. For the phase images, the following processing steps were performed: “base flatten”, “align rows” with the selection mean of differences, “remove scars”, “polynomial background”, set minimum value as zero point (“fix zero”).

Electrochemical measurements: For square wave voltammetry (SWV) measurement, a grounded ZAHNER ZENNIUM pro electrochemical workstation controlled *via* THALES software was used. The electrochemical cell was positioned inside a Faraday cage during the measurement. The electrochemical cell has got three screw openings for inserting the electrodes and a gas inlet. As working electrode, a glassy carbon plate (45 mm x 2.2 mm x 1 mm, partially immersed) bare or coated with the respective MPEGC₆₀ thin film was used, as counter electrode a platinum spiral and as reference electrode a leakless miniature Ag/AgCl electrode from eDAQ. All electrodes were put through a septum, the glassy carbon plate was hold by a flat copper crocodile clip. The SWV measurement was carried out under Argon flow in TBABF₄ (tetrabutylammonium tetrafluoroborate: 99 % purity, Sigma Aldrich, recrystallized once in deionized water, dried and stored under argon atmosphere before usage) (0.06 M in MeOH (Thermo ScientificTM, ACROS OrganicsTM, 99.8 %, extra dry, over molecular sieves, AcroSeal[®])) with Ferrocene as internal standard and reference for

determining the LUMO energy levels. Negative scans were running from +0.4 to -1.3 V vs. Ag/AgCl, positive scans were running from +0.4 to +1.0 V vs. Ag/AgCl (eDAQ). Negative as well as positive scans were carried out with 10 Hz frequency, 50 mV amplitude, 2 mV step, 25 ms integration time. The sampling procedure consisted of two negative scans, followed by two positive scans and one or two negative scans.

Data processing was carried out by a Mathematica routine. Second cathodic scan was subtracted from first cathodic scan, followed by an offset correction for both cathodic and anodic scan. The current density was determined by applying the area of active layer deduced from the measured immersion depth of the glassy carbon plate electrode. The maximum of the first reduction potential of MPEGC₆₀ in the thin films of different deposition parameters was determined *via* peak fits, also applied to the ferrocene to ferrocenium (Fc/Fc⁺) oxidation peak.

The respective LUMO (Lowest Unoccupied Molecular Orbital) energies [eV vs. vacuum energy level] were determined via the following equation:

$$E_{LUMO} = - \left[E_{\text{absolute potential}} \left(\frac{Fc}{Fc^+} \right) - E_{\frac{1}{2}}^{\text{ox}} \left(\frac{Fc}{Fc^+} \right) + E_{\frac{1}{2}}^{\text{red}} (MPEGC_{60}) \right] [eV]^{[27]}, \text{ with maximum redox response}^{[28]}$$

consideration instead of its respective onset^[27] as detailed in the SI (chapter 3).

$E_{\text{absolute potential}}(Fc/Fc^+)$: 5.1 V^[27] as detailed in the SI (chapter 3.3).

Repetition measurements were carried out to ensure the global trend.

Density functional theory calculations: Quantum chemical structure optimizations along with the calculations of electron densities^[29] and electrostatic potentials were carried out using density functional theory (DFT) as implemented in the GPU-accelerated program TeraChem^[30]. Valence double- ζ basis set Ahlrichs- pVDZ with polarization functions on all atoms as introduced by Ahlrichs and co-workers^[31] was used to optimize the geometries for all the molecules, whereas electrostatic potentials were calculated with the triple- ζ basis set 6-311++G^[32] [33]. Hybrid functional B3LYP^[34] was used for all calculations, with Grimme's D3 dispersion correction^[36] enabled. Electrostatic potentials ranging on a color scale of -0.08 to 0.08 units were plotted on the electron density iso-surface of 0.0001 a.u.

Statistical analysis:

- $\Pi(A)$ isotherms: See SI chapter 9: "Statistical analysis of the MPEGC₆₀ $\Pi(A)$ -isotherm"
- Reduction potentials: See data evaluation routines in SI sections "3. Square-wave voltammetry (SWV) data" and "Summary of MPEGC₆₀ model layer system SWV investigation..."
- $N^{\text{surface}}/N^{\text{total}}$ calculations: See SI section 7 "N^{surface}/N^{total} calculations" (Table SI 2 and Table SI 3)
- $E_{\text{LUMO}}^{\text{mean}}$ vs. $N^{\text{surface}}/N^{\text{total}}$ ratios: See SI section 8 "E^{mean}_{LUMO} vs. N^{surface}/N^{total}" (Table SI 4)

Details of processing of UV-vis, AFM, TEM and GIWAXS data are provided in the section "Supramolecular structure and morphological characterization".

SUPPORTING INFORMATION

Supporting Information is available from the Wiley Online Library or from the author.

ACKNOWLEDGEMENT

S.J.F. and M.P. acknowledge funding from the Deutsche Forschungsgemeinschaft, DFG (German Research Foundation), (Project B09 within the Sonderforschungsbereich SFB/TRR 234 "Catalight", project ID: 364549901). M.P. acknowledges funding from BMWI (ZIM project 217090). F.H.S. and J.E. are grateful for funding from the Deutsche Forschungsgemeinschaft, DFG (German Research Foundation), (Project B05 within the Sonderforschungsbereich SFB/TRR 234 "Catalight", project ID: 364549901). The TEM/cryo-TEM facilities of the Jena Center for Soft Matter (JCSM) were established with a grant from the DFG (German Research Foundation) and the EFRE (European Funds for Regional Development). We are grateful for fruitful discussions and support by Dr. Mathias Micheel, Yves Carstensen, Andreas Berger, Dr. Stephanie Höppener, and Dr. Martin Schulz. This research used resources of the Advanced Photon Source, a U.S. Department of Energy (DOE) Office of Science user facility operated for the DOE Office of Science by Argonne National Laboratory. K.G. and E. J. A. acknowledge funding from U.S. Department of Energy (DOE), Office of Science, Office of Basic Energy Science, Division of Chemical Sciences, Geosciences and Biosciences, through Argonne National Laboratory under Contract No. DE-AC02-06CH11357.

CONFLICT OF INTEREST

The authors declare no conflict of interest.

DATA AVAILABILITY STATEMENT

The data that support the findings of this study are available from the corresponding author upon reasonable request.

REFERENCES

- [1] a)K. Zhou, J. Xin, W. Ma, *ACS Energy Letters* **2019**, 4, 447; b)K. Zhou, Y. Liu, A. Alotaibi, J. Yuan, C. Jiang, J. Xin, X. Liu, B. A. Collins, F. Zhang, W. Ma, *ACS Energy Letters* **2020**, 5, 589; c)X. Song, N. Gasparini, L. Ye, H. Yao, J. Hou, H. Ade, D. Baran, *ACS Energy Letters* **2018**, 3, 669; d)S. Li, L. Zhan, F. Liu, J. Ren, M. Shi, C.-Z. Li, T. P. Russell, H. Chen, *Advanced Materials* **2018**, 30, 1705208; e)H. Lee, C. Park, D. H. Sin, J. H. Park, K. Cho, *Advanced Materials* **2018**, 30, 1800453; f)X. Jiao, L. Ye, H. Ade, *Advanced Energy Materials* **2017**, 7, 1700084; g)H. Kang, W. Lee, J. Oh, T. Kim, C. Lee, B. J. Kim, *Accounts of Chemical Research* **2016**, 49, 2424.
- [2] a)C. Yang, J. Zhang, N. Liang, H. Yao, Z. Wei, C. He, X. Yuan, J. Hou, *Journal of Materials Chemistry A* **2019**, 7, 18889; b)H. Bronstein, C. B. Nielsen, B. C. Schroeder, I. McCulloch, *Nature Reviews Chemistry* **2020**, 4, 66.
- [3] a)L. Meng, Y. Zhang, X. Wan, C. Li, X. Zhang, Y. Wang, X. Ke, Z. Xiao, L. Ding, R. Xia, H.-L. Yip, Y. Cao, Y. Chen, *Science* **2018**, 361, 1094; b)M. A. Green, Y. Hishikawa, E. D. Dunlop, D. H. Levi, J. Hohl-Ebinger, M. Yoshita, A. W. Y. Ho-Baillie, *Progress in Photovoltaics: Research and Applications* **2019**, 27, 3; c)Q. Liu, Y. Jiang, K. Jin, J. Qin, J. Xu, W. Li, J. Xiong, J. Liu, Z. Xiao, K. Sun, S. Yang, X. Zhang, L. Ding, *Science Bulletin* **2020**, 65, 272; d)Y. Su, L. Zhang, Z. Ding, Y. Zhang, Y. Wu, Y. Duan, Q. Zhang, J. Zhang, Y. Han, Z. Xu, R. Zhang, K. Zhao, S. Liu, *Advanced Energy Materials* **2022**, 12, 2103940; e)F. Liu, L. Zhou, W. Liu, Z. Zhou, Q. Yue, W. Zheng, R. Sun, W. Liu, S. Xu, H. Fan, L. Feng, Y. Yi, W. Zhang, X. Zhu, *Advanced Materials* **2021**, 33,

- 2100830; f)C. Li, J. Zhou, J. Song, J. Xu, H. Zhang, X. Zhang, J. Guo, L. Zhu, D. Wei, G. Han, J. Min, Y. Zhang, Z. Xie, Y. Yi, H. Yan, F. Gao, F. Liu, Y. Sun, *Nature Energy* **2021**, 6, 605.
- [4] a)K. R. Graham, C. Cabanetos, J. P. Jahnke, M. N. Idso, A. El Labban, G. O. N. Ndjawa, T. Heumueller, K. Vandewal, A. Salleo, B. F. Chmelka, A. Amassian, P. M. Beaujuge, M. D. McGehee, *Journal of the American Chemical Society* **2014**, 136, 9608; b)A. M. Levine, S. Biswas, A. B. Braunschweig, *Nanoscale Advances* **2019**, 1, 3858.
- [5] a)S. H. Yu, K. H. Park, Y.-H. Kim, D. S. Chung, S.-K. Kwon, *Macromolecules* **2017**, 50, 4227; b)S. W. Kim, Y. J. Lee, Y. W. Lee, C. W. Koh, Y. Lee, M. J. Kim, K. Liao, J. H. Cho, B. J. Kim, H. Y. Woo, *ACS Applied Materials & Interfaces* **2018**, 10, 39952; c)X. Wang, H. Lu, J. Zhou, X. Xu, C. e. Zhang, H. Huang, J. Song, Y. Liu, X. Xu, Z. Xie, Z. Tang, Z. Bo, *ACS Applied Materials & Interfaces* **2021**, 13, 39652; d)Y. Liu, C. e. Zhang, D. Hao, Z. Zhang, L. Wu, M. Li, S. Feng, X. Xu, F. Liu, X. Chen, Z. Bo, *Chemistry of Materials* **2018**, 30, 4307.
- [6] X. Gu, L. Shaw, K. Gu, M. F. Toney, Z. Bao, *Nat Commun* **2018**, 9, 534.
- [7] C. Poelking, M. Tietze, C. Elschner, S. Olthof, D. Hertel, B. Baumeier, F. Würthner, K. Meerholz, K. Leo, D. Andrienko, *Nature Materials* **2015**, 14, 434.
- [8] a)J. R. Tumbleston, B. A. Collins, L. Q. Yang, A. C. Stuart, E. Gann, W. Ma, W. You, H. Ade, *Nature Photonics* **2014**, 8, 385; b)S. Das, J. Preiss, J. Plentz, U. Bruckner, M. von der Luhe, O. Eckardt, A. Dathe, F. H. Schacher, E. Tauscher, U. Ritter, A. Csaki, G. Andra, B. Dietzek, M. Presselt, *Advanced Energy Materials* **2018**, 8, 1801737.
- [9] a)T. E. Shubina, D. I. Sharapa, C. Schubert, D. Zahn, M. Halik, P. A. Keller, S. G. Pyne, S. Jennepalli, D. M. Guldi, T. Clark, *Journal of the American Chemical Society* **2014**, 136, 10890; b)I. Fernández Torrente, K. J. Franke, J. I. Pascual, *Journal of Physics: Condensed Matter* **2008**, 20, 184001.
- [10] a)Y. Yang, F. Arias, L. Echegoyen, L. P. F. Chibante, S. Flanagan, A. Robertson, L. J. Wilson, *Journal of the American Chemical Society* **1995**, 117, 7801; b)D. Dubois, K. M. Kadish, S. Flanagan, R. E. Haufler, L. P. F. Chibante, L. J. Wilson, *Journal of the American Chemical Society* **1991**, 113, 4364.
- [11] a)I. Langmuir, *Journal of the American Chemical Society* **1917**, 39, 1848; b)I. Langmuir, K. B. Blodgett, *Kolloid-Zeitschrift* **1935**, 73, 257.
- [12] a)M. L. Hupfer, M. Kaufmann, F. Herrmann-Westendorf, T. Sachse, L. Roussille, K. H. Feller, D. Weiss, V. Deckert, R. Beckert, B. Dietzek, M. Presselt, *ACS Appl Mater Interfaces* **2017**, 9, 44181; b)M. L. Hupfer, S. Ghosh, Y. C. Wang, T. Opsomer, T. G. Mayerhofer, W. Dehaen, M. Presselt, *Advanced Materials Interfaces* **2022**, 9, 2101490.
- [13] a)G. Zhavnerko, G. Marletta, *Materials Science and Engineering B-Advanced Functional Solid-State Materials* **2010**, 169, 43; b)X. Li, J. F. Gilchrist, *Langmuir* **2016**, 32, 1220; c)M. Parchine, J. McGrath, M. Bardosova, M. E. Pemble, *Langmuir* **2016**, 32, 5862; d)M. Parchine, T. Kohoutek, M. Bardosova, M. E. Pemble, *Solar Energy Materials and Solar Cells* **2018**, 185, 158; e)L. Xu, A. R. Tetreault, H. H. Khaligh, I. A. Goldthorpe, S. D. Wettig, M. A. Pope, *Langmuir* **2019**, 35, 51; f)T. R. Hayes, E. N. Lang, A. Shi, S. A. Claridge, *Langmuir* **2020**, 36, 10577.
- [14] S. Das, F. Herrmann-Westendorf, F. H. Schacher, E. Tauscher, U. Ritter, B. Dietzek, M. Presselt, *ACS Appl Mater Interfaces* **2016**, 8, 21512.
- [15] J. T. Davies, E. K. Rideal, in *Interfacial Phenomena (Second Edition)*, (Eds: J. T. Davies, E. K. Rideal), Academic Press, 1961.
- [16] G. L. Gaines, I. Prigogine, *Insoluble Monolayers at Liquid-gas Interfaces - chapter 4: Properties of Monolayer Films*, Interscience Publishers, **1966**.
- [17] a)M. L. Hupfer, D. Blaschke, H. Schmidt, M. Presselt, *Langmuir* **2021**, 37, 13255; b)A. Chachaj-Brekiesz, J. Kobierski, A. Wnętrzak, P. Dynarowicz-Latka, *Membranes* **2021**, 11, 53; c)M. L. Hupfer, R. Meyer, T. Deckert-Gaudig, S. Ghosh, A. Skabeev, K. Peneva, V. Deckert, B. Dietzek, M. Presselt, *Langmuir* **2021**, 37, 11018.

- [18] S. Wang, R. M. Leblanc, F. Arias, L. Echegoyen, *Langmuir* **1997**, 13, 1672.
- [19] a)K. B. Blodgett, *Journal of the American Chemical Society* **1934**, 56, 495; b)K. B. Blodgett, *Journal of the American Chemical Society* **1935**, 57, 1007.
- [20] a)Y. Tabe, K. Ikegami, M. Sugi, *Journal of Applied Physics* **1993**, 73, 905; b)J. G. Byatt-Smith, B. R. Malcolm, *Journal of the Chemical Society, Faraday Transactions* **1994**, 90, 493; c)B. R. Malcolm, *Journal of Physics E: Scientific Instruments* **1988**, 21, 603.
- [21] I. Langmuir, V. J. Schaefer, *Journal of the American Chemical Society* **1938**, 60, 1351.
- [22] M. L. Hupfer, J. Dellith, M. Seyring, M. Diegel, A. Dellith, S. Ghosh, M. Rettenmayr, B. Dietzek-Ivansic, M. Presselt, *Advanced Materials* **2023**, 35, e2204874.
- [23] a)S. Hellström, L. J. Lindgren, Y. Zhou, F. Zhang, O. Inganäs, M. R. Andersson, *Polymer Chemistry* **2010**, 1, 1272; b)D. Gudeika, R. Lygaitis, V. Mimitè, J. V. Grazulevicius, V. Jankauskas, M. Lapkowski, P. Data, *Dyes and Pigments* **2011**, 91, 13; c)A. Bayat, E. Saievar-Iranizad, *Journal of Luminescence* **2017**, 192, 180.
- [24] D. M. DeLongchamp, R. J. Kline, D. A. Fischer, L. J. Richter, M. F. Toney, *Advanced Materials* **2011**, 23, 319.
- [25] Z. Jiang, X. Li, J. Strzalka, M. Sprung, T. Sun, A. R. Sandy, S. Narayanan, D. R. Lee, J. Wang, *Journal of Synchrotron Radiation* **2012**, 19, 627.
- [26] Z. Jiang, *Journal of Applied Crystallography* **2015**, 48, 917.
- [27] C. M. Cardona, W. Li, A. E. Kaifer, D. Stockdale, G. C. Bazan, *Advanced Materials* **2011**, 23, 2367.
- [28] a)J. Sworakowski, J. Lipiński, K. Janus, *Organic Electronics* **2016**, 33, 300; b)M. Kubo, H. Yoshida, *Organic Electronics* **2022**, 106551.
- [29] a)M. Presselt, C. Schnedermann, M. Muller, M. Schmitt, J. Popp, *Journal of Physical Chemistry A* **2010**, 114, 10287; b)M. Presselt, C. Schnedermann, M. Schmitt, J. Popp, *J Phys Chem A* **2009**, 113, 3210.
- [30] a)I. S. Ufimtsev, T. J. Martinez, *Journal of Chemical Theory and Computation* **2009**, 5, 2619; b)C. M. Isborn, N. Luehr, I. S. Ufimtsev, T. J. Martinez, *Journal of Chemical Theory and Computation* **2011**, 7, 1814; c)A. V. Titov, I. S. Ufimtsev, N. Luehr, T. J. Martinez, *Journal of Chemical Theory and Computation* **2013**, 9, 213; d)C. Song, L.-P. Wang, T. J. Martínez, *Journal of Chemical Theory and Computation* **2016**, 12, 92; e)W. Beenken, W. Maes, M. Kruk, T. Martínez, M. Presselt, *The Journal of Physical Chemistry A* **2015**, 119, 6875; f)D. M. Gampe, M. Kaufmann, D. Jakobi, T. Sachse, M. Presselt, R. Beckert, H. Görls, *Chemistry* **2015**, 21, 7571; g)C. M. Isborn, N. Luehr, I. S. Ufimtsev, T. J. Martínez, *Journal of Chemical Theory and Computation* **2011**, 7, 1814; h)J. Preiß, M. Jäger, S. Rau, B. Dietzek, J. Popp, T. Martínez, M. Presselt, *ChemPhysChem* **2015**, 16, 1395; i)J. Preiß, F. Herrmann-Westendorf, T. H. Ngo, T. J. Martínez, B. Dietzek, J. P. Hill, K. Ariga, M. M. Kruk, W. Maes, M. Presselt, *The Journal of Physical Chemistry A* **2017**, 121, 8614; j)J. Preiß, D. Kage, K. Hoffmann, T. J. Martínez, U. Resch-Genger, M. Presselt, *The Journal of Physical Chemistry A* **2018**, 122, 9813; k)T. Sachse, T. J. Martinez, M. Presselt, *The Journal of Chemical Physics* **2019**, 150, 174117.
- [31] A. Schäfer, H. Horn, R. Ahlrichs, *The Journal of Chemical Physics* **1992**, 97, 2571.
- [32] R. Krishnan, J. S. Binkley, R. Seeger, J. A. Pople, *Journal of Chemical Physics* **1980**, 72, 650.
- [33] T. Clark, J. Chandrasekhar, G. W. Spitznagel, P. v. R. Schleyer, *Journal of computational chemistry* **1983**, 4.
- [34] P. J. Stephens, F. J. Devlin, C. F. Chabalowski, M. J. Frisch, *The Journal of Physical Chemistry* **1994**, 98, 11623.
- [35] T. Yanai, D. P. Tew, N. C. Handy, *Chem. Phys. Lett.* **2004**, 393, 51.
- [36] a)S. Grimme, J. Antony, S. Ehrlich, H. Krieg, *The Journal of Chemical Physics* **2010**, 132, 154104; b)S. Das, J. Fiedler, O. Stauffert, M. Walter, S. Y. Buhmann, M. Presselt, *Physical chemistry chemical physics : PCCP* **2020**, 22, 23295.

Figure 1: Panel (a): Compressional modulus of MPEGC₆₀ (blue) and stearic acid (gray) as reference; Panel (b): Langmuir isotherm of MPEGC₆₀ and stearic acid (SA), surface pressures used for deposition and the corresponding mean molecular areas (red dots), Lewis structure of MPEGC₆₀ together with a picture of the electrostatic potential distribution at a smoothed van der Waals surface; Panel (c): Illustrations of possible MPEGC₆₀ assemblies at the air-water interface that are in agreement with the mean molecular areas at deposition.

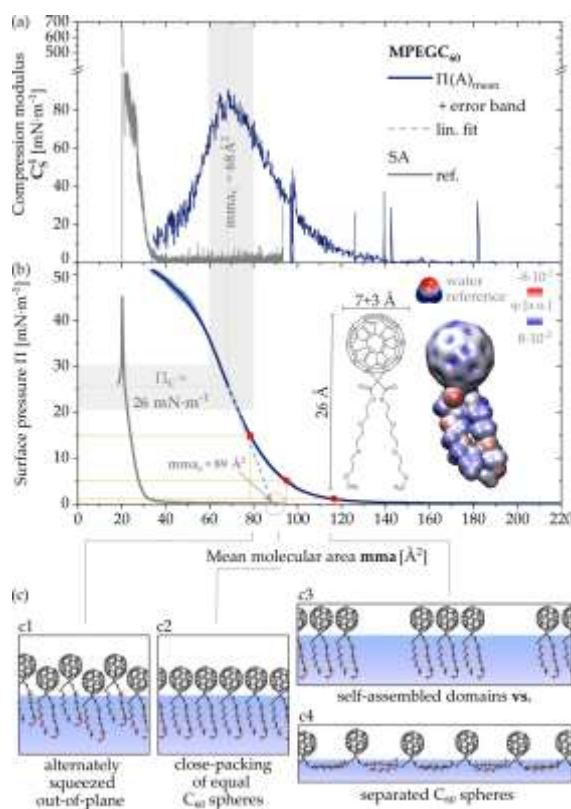


Figure 2: (a) Rolling transferred Langmuir layer (rtLL) deposition setup; (b) Magnified view of the role with mounted substrates. (c,d) Schematic representation of the rtLL deposition process.

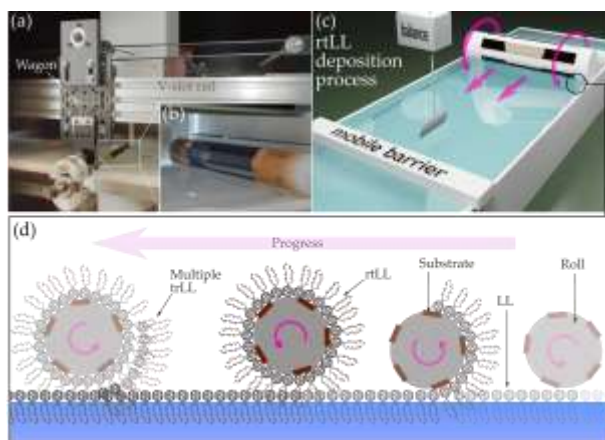


Figure 3: Reduction potentials of MPEGC₆₀ layers as function of surface pressure at deposition Π_{rtLL} and number of rolling transferred Langmuir layers (#rtLL). The data points at identical Π_{rtLL} - and #rtLL-values refer to repeat measurements on different samples. The error bars are obtained from peak fits of the electrochemical reduction peaks.

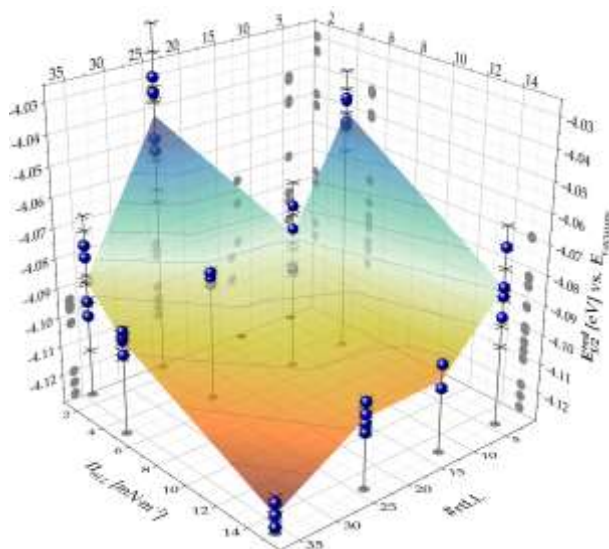


Figure 4: AFM images (a) – (g) for different rtLL films. (a), (b) and (d) layer stack deposited on quartz glass substrate with a monolayer stearic acid below (c) and (e) – (g) layer stack deposited on glassy carbon plate. Ratio number of surface sites to the number of total sites ($N_{\text{surface}}/N_{\text{total}}$) (center) as a function of the surface pressure Π_{rtLL} and the number of rolling transferred Langmuir layers (#rtLL) of which the organic thin film layer-stack consists of. The ratios are calculated by considering mean molecular areas as determined by the surface pressure at deposition (blue spheres) and as measured via UV-vis absorption spectroscopy (orange spheres), thus enabling determination of error bars.

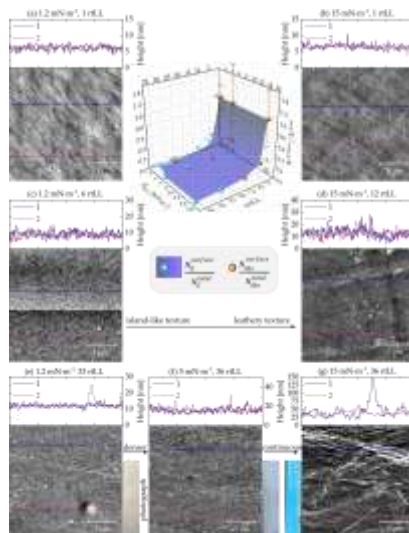
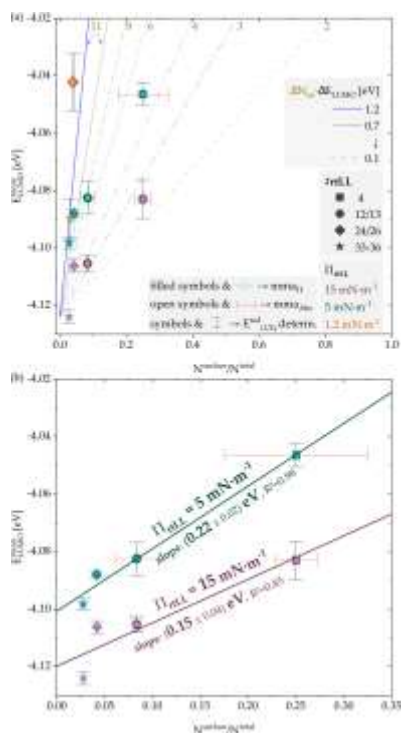


Figure 5: Panel (a): E_{LUMO}^{mean} plotted as a function of $N_{surface}/N_{total}$ according Eq. 10 using $\Delta E_{LUMO} = 65$ meV (grey lines), 109 meV (blue line). The different slopes of the $E_{LUMO}^{mean}(x)$ graphs result from the different $\Delta N_{nn}\Delta E_{LUMO}$ parameters. Open symbols and horizontal error bars refer to $N_{surface}/N_{total}$ ratios calculated from surface concentrations deduced from UV-vis absorption spectra. Filled symbols refer to $N_{surface}/N_{total}$ ratios calculated from isotherm-determined m_{mm} , i.e., depending on the number of layers only. Panel (b): Zoom of the data shown in panel (a) including line fits.



This article is protected by copyright. All rights reserved.

TOC

A rolling transfer of Langmuir layers of amphiphilic C60 derivatives is shown to enable the production of films with highly defined morphology. The resulting systematically tuned lowest unoccupied molecular orbital (LUMO) energies enable the establishment of a practical model that functionally relates the LUMO energies to a morphological descriptor. This allows prediction of the range of experimentally accessible LUMO energies.

